Measurement 199 (2022) 111534

Contents lists available at ScienceDirect

Measurement

journal homepage: www.elsevier.com/locate/measurement

ANN-based estimation of MEMS diaphragm response: An application for three leaf clover diaphragm based Fabry-Perot interferometer

Enes Yigit [a,b], Şekip Esat Hayber [c], Umut Aydemir [a,b,d,*]

[a] Department of Electrical-Electronics Engineering, Bursa Uludağ University, Bursa, Turkey
[b] Optics and Photonics Engineering, Bursa Uludağ University, Bursa, Turkey
[c] Department of Electrical-Electronics Engineering, Kırşehir Ahi Evran University, Kırşehir, Turkey
[d] National Nanotechnology Research Center – UNAM, Bilkent University, Ankara, Turkey

ARTICLE INFO

Keywords:
Machine learning
MEMS
Diaphragm Design
FEM
Fabry-Perot interferometer

ABSTRACT

In this study, an artificial neural network (ANN) based model is developed for MEMS diaphragm analysis, which does not require difficult and time-consuming FEM processes. ANN-based estimator is generated for static pressure response (*d*) and dynamic pressure response (*f*) analysis of TLC (three leaf clover) diaphragms for Fabry-Perot interferometers as an example. TLC is one of the unsealed MEMS design diaphragms formed by three leaves of equal angles. The diaphragms used to train ANNs are designed with SOLIDWORKS and analyzed with ANSYS. A total of 1680 TLC diaphragms are simulated with eight diaphragm parameters (3 for SiO_2 material, 4 for geometry, and 1 for pressure) to create a data pool for ANN's training, validation, and testing processes. 80% of the data is used for training, 15% for validation, and the remaining for testing. Only four geometric parameters are used as input in the ANN estimator, and the material parameters are added to the model with an analytical multiplier. Thus, network models that estimate *d* and *f* values for all kinds of diaphragm materials are proposed, with a material-independently trained ANN structure. The performance of the ANN model is compared with the empirical equation suggested in the literature, and its superiority is demonstrated. In addition, the *d* and *f* parameters of TLC diaphragms designed with five different materials (Si, In_2Se_3, Ag, EPDM, Graphene) are estimated to be very close to the real ones. By using the proposed method, analyses of TLC diaphragms are quickly performed without the need for time-consuming and costly design and analysis programs.

1. Introduction

Interferometer-based fiber optic sensors effectively measure physical quantities such as pressure, vibration, and temperature, especially in harsh environmental conditions [1,2]. Among these sensors, diaphragm-based Fabry-Perot sensors stand out with their advantages: high sensitivity, no reference arm, the practicality of use, flexible design, and low-cost production [3-6]. The performance of diaphragm-based sensors can be determined by the diaphragm design. The most critical parameters affecting the performance are linearity, tunability, sensitivity, and operating range [7-10]. These parameters are determined by static pressure response (*d*) and dynamic pressure response (*f*) analysis, which are two essential characteristics of the diaphragm [11]. It is essential to design sensors at the desired frequency and sensitivity values. High-sensitivity and narrowband sensors should be operated close to the resonant frequency. A flat frequency response over a wide range is desired in broadband applications.

Circular diaphragms are the most widely used diaphragm geometry in the literature [12-15]. Circular geometries are preferred because they are well-matched with typical cylindrical fiber apparatus (e.g., ceramic ferrules), and mathematical models are available [12-15]. The frequency response and sensitivity can be controlled by either changing the geometry [4,6,7,9-11,13-15] or material [4-15] of the diaphragm. Since there is a limit on the materials used in the manufacture of diaphragms in the literature, design diaphragms with different sensitivity degrees and frequency responses are needed. For this reason, researchers in the literature tend toward novel design-diaphragm (DD) geometries [16-20]. DDs have more geometric parameters than conventional diaphragms. Therefore, sensor tips with different sensitivity levels can be manufactured when changing the diaphragm thickness and diameter is impossible. In the literature, DDs types are available such as three-leaf clover (TLC) [16], beam supported membrane [17], corrugated

* Corresponding author.
E-mail address: umutaydemir@uludag.edu.tr (U. Aydemir).

https://doi.org/10.1016/j.measurement.2022.111534
Received 22 March 2022; Received in revised form 10 June 2022; Accepted 20 June 2022
Available online 23 June 2022

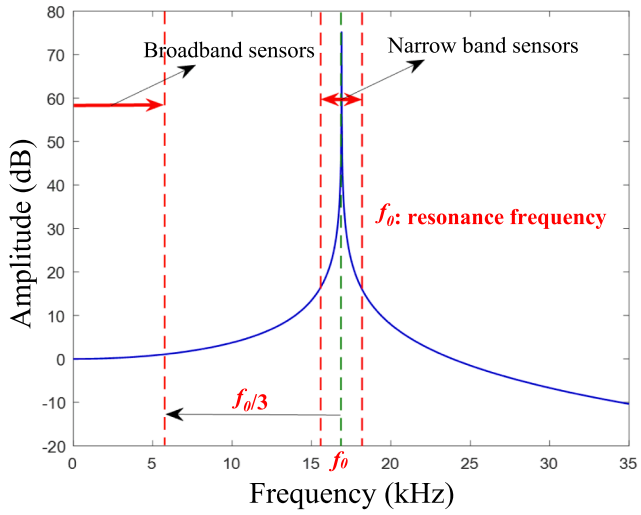

Fig. 1. Narrow and broadband representation according to the resonance frequency of the diaphragm.

diaphragm [18], center-embossed diaphragm [19], and fungus-shaped center embossed diaphragm [20].

In order to measure the acoustic pressure in a liquid or gas-filled environment, it is not possible to balance the internal and external pressure by itself, regardless of the location of the sensor, in classical sealed diaphragms. In early studies, researchers were able to take measurements by balancing the internal pressure with the external pressure using a cantilever structure [21]. Since this cantilever structure has some disadvantages, the BSM structure was later inspired by this structure. Using the BSM structure, it was possible to measure the acoustic pressure caused by the partial discharge of transformer oils [22-24]. Thus, acoustic pressure-sensitive sensor tips, which are senseless from gas and liquid pressures of the environment, have been developed. Another group used BSM-like flywheel unsealed-diaphragm structures on the Fabry-Perot interferometer to detect acoustic pressure [25,26]. As understood from these studies, it is a problem to perceive the external pressures in the environment by balancing the internal and external pressure. To solve this problem, the use of unsealed DDs has been suggested in the literature. Thanks to these structures, the production of self-calibrated sensor tips became possible. In addition, it is seen that such diaphragms are used not only in Fabry-Perot interferometers but also in sensor assemblies based on different methods [27,28]. Each DD structure provides significant advantages to increase the performance of the sensor. However, these DDs do not have an accepted mathematical model like conventional diaphragms. Therefore, a large number of three-dimensional (3D) designs and finite element method (FEM) based analyses of these designs are needed to understand the sensor performance of DDs. The FEM-based analysis of these structures is quite long and tedious. This challenging analysis process can be predicted with high accuracy with the help of machine learning (ML) based algorithms without requiring FEM-based analysis.

In recent years, some nonlinear problems can be solved by using ML algorithms without the need for time-consuming and costly software. However, the performance of the solution does not only depend on the method used, but also changes according to the problem parameters. In [29], the operating frequency of the C-shaped antenna structure is estimated by employing the K-nearest neighbor (KNN) algorithm without the need for 3D antenna design software. In [30], the resonance frequency of the T-shaped microstrip antenna is estimated with artificial neural networks (ANN). A recent study demonstrates that ML algorithms can recognize surface roughness in fiber optic tactile sensors [31]. In [32], ML is used for geometry optimization of molecular simulations for density functional theory. In [33], ML algorithms accelerate FEM-based biomechanical simulations. These and similar studies have shown that the target parameters of unique designs can be successfully estimated by applying ML methods and without the need for long design processes.

In this study, the ANN-based parameter estimation method is proposed for the first time to analyze DDs. With the help of the proposed method, f and d parameters of TLC diaphragms of different geometric sizes are estimated without costly design and simulation software. Since the proposed method is designed independently of the diaphragm material, f and d values are predicted with high success for different materials. The networks are trained using the f and d results obtained with FEM for only the SiO_2 diaphragm. Then the results are expanded to estimate for Si, Ag, In_2Se_3, EPDM, and graphene TLC diaphragms by the proposed method. The outline of this study is as follows. In the second section, general mathematical equations of TLC diaphragms and proposed ANN structure are presented in detail. In the third section, the obtained results are compared with those in the literature. The performance and superiority of the proposed method are revealed. The study is summarized in the last section.

2. Materials and methods

2.1. Structure of the TLC diaphragms

Circular diaphragms do not need FEM analysis as they have analytical formulas [9-11,13-15]. They are widely used because the sensitivity and frequency response of the diaphragm can be easily calculated. According to the literature, decreasing the diaphragm thickness' is a process that increases sensitivity, but this cannot be appropriate for every diaphragm material. Moreover, producing the most commonly used silicon (Si) or silica (SiO_2) diaphragms with a thickness of less than one micrometer is a complicated process [34,35]. Another way to increase sensitivity is to increase the radius of the diaphragm [10,16]. However, this means large-diameter sensing tips and is not helpful for miniaturization. In addition, the size of the diaphragm is determined by the inner diameter of the standard ceramic ferrule (125 μm). Therefore, many studies do not take advantage of the influence of diameter on frequency and sensitivity [35,36].

For this reason, DDs are needed because they allow tuning with extra parameters other than thickness and radius. Thanks to the developing micro and nano electro-mechanical system (MEMS/NEMS) techniques, it is easy to produce precision diaphragms in desired geometries [24]. For this reason, narrowband tuning, which is more difficult in traditional diaphragms, has become easier with DDs. The representation of narrow and broadband sensors according to the resonance frequency is given in Fig. 1. In addition, the schematic representation of the sensor structure based on the diaphragm-based Fabry-Perot interferometer is depicted in Fig. 2.

In Fig. 2, the first interface of the Fabry-Perot interferometer is fiber-air (R_1), and the second interface is the air-diaphragm (R_2). The phase difference between the optical waves guided back to the fiber by passing through both interfaces is given in $\varphi = 4\pi nL/\lambda$ [2,3]. Here, n is the refractive index of the cavity, L is the length of the cavity, and λ is the wavelength of the light source. Thus, the diaphragm deflected by external influence will change the optical path of the interferometer. The optical intensity at the output is correlated with the physical parameters to be measured. Thanks to the TLC-like unsealed diaphragm structures seen in the figure, the internal pressure is balanced with the external pressure, making the sensor sensitive to the acoustic pressure in the environment [21-27].

The TLC structure shown in Fig. 3 is an excellent example of DDs [16]. This structure has two prominent advantages over the classical circular diaphragms:

1. It can be used in any media with pressure differences thanks to the gaps in its structure.
2. It has a high tunable feature as it contains more parameters.

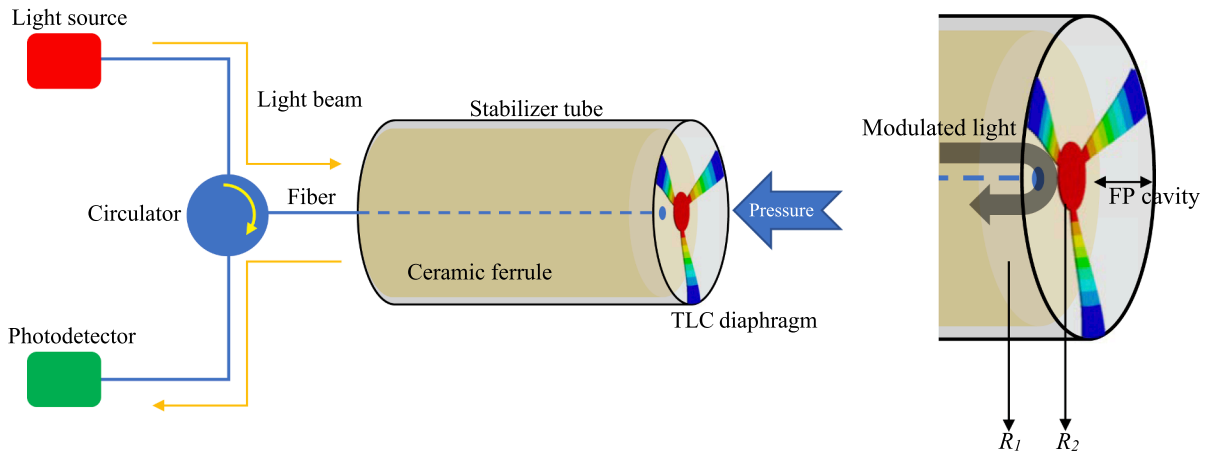

Fig. 2. Schematic representation of the TLC diaphragm-based Fabry-Perot interferometer.

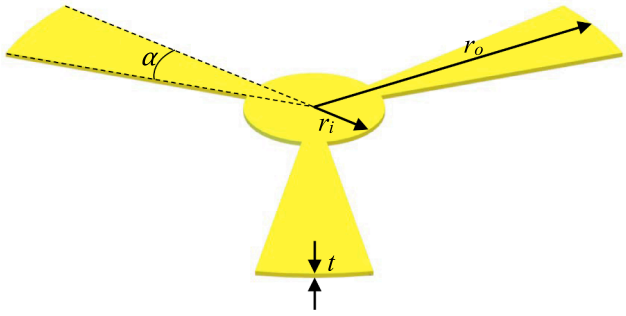

Fig. 3. TLC diaphragm structure with four geometric parameters.

Table 1
The parameters of designed TLC diaphragms for SiO_2.

Geometric Parameters	Variation range	# of variation
t	5 μm – 20 μm	4
r_o	0.3 mm – 0.7 mm	5
r_i	0.05 mm – 0.65 mm	7
α	10°–120°	12
Number of total designs		1680

There is no exact analytical formula in the literature for TLC structure with outer radius r_o, inner radius r_i, thickness t, and leaf angle α. However, in a recently published study [16], an equation developed using the analytical equations of circular diaphragms and valid only for the $r_i = r_o/2$ condition is given.

The d and f equations of a circular diaphragm are given below.

$$d = d_m \times \frac{3r_o^4}{16t^3} \tag{1}$$

$$d_m = \frac{P(1-\nu^2)}{E} \tag{2}$$

$$f = f_m \times \frac{10.21t}{2\sqrt{12}\pi {r_o}^2} \tag{3}$$

$$f_m = \sqrt{\frac{E}{\rho(1-\nu^2)}} \tag{4}$$

Here, E, ρ, and ν are Young's modulus, mass density, and Poisson's ratio of the material, respectively. P is the pressure applied to the diaphragm, and its unit is Pascal. When Eq. (1) and (3) are examined, it is seen that the first part of both equations consists entirely of material

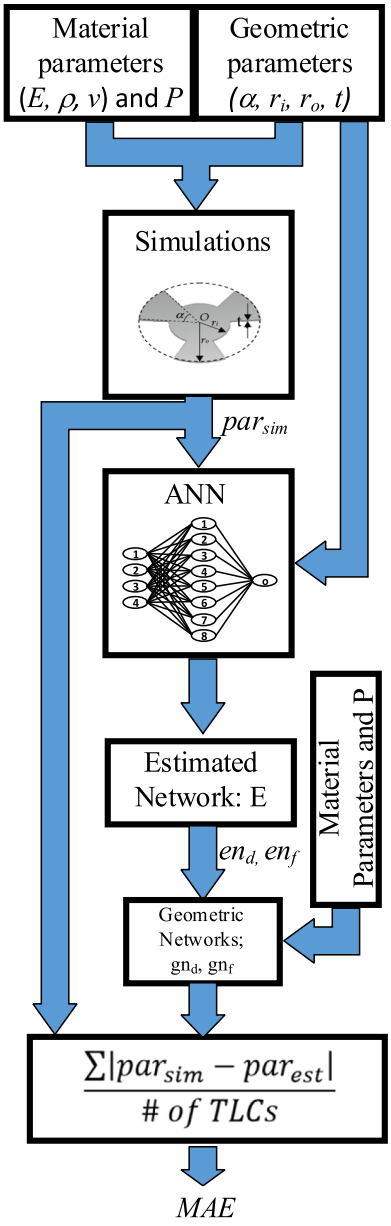

Fig. 4. Working principle of ANN-based estimator.

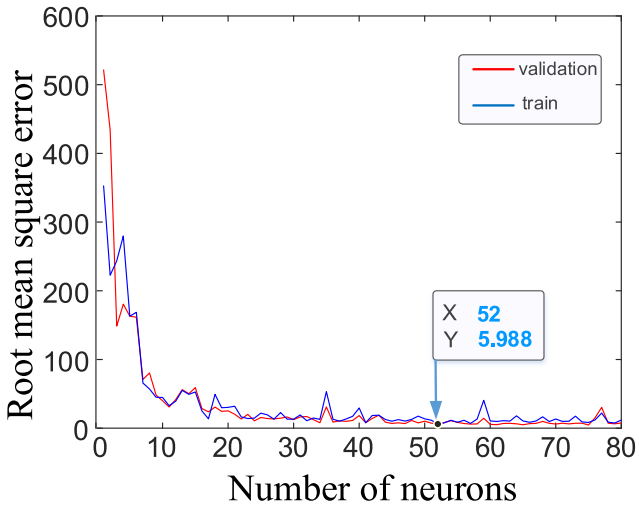

Fig. 5. The performance of the ANN for the number of neurons.

Table 2
The parameters used to set the ANN model.

Parameters	Set type/Value
Data Division	Random
Training	Levenberg-Marquardt
Number of epochs	1000
Minimum gradient descent	1×10^{-7}
Momentum parameter (μ)	0.0001
μ increment value	5
μ decrement value	0.15
Maximum μ value	10×10^{10}

properties (d_m and f_m), and the second part consists of coefficients depending on the geometry of the diaphragm. In [16], d and f values are defined empirically for TLC diaphragms with limited geometries ($r_i = r_o/2$).

$$d_{TLC} = d_m \times \frac{3r_o^4}{16t^3\sqrt{\alpha/120^\circ}};\ r_i = r_o \Big/ 2 \tag{5}$$

$$f_{TLC} = f_m \times \frac{10.21t(\alpha/120^\circ)^{1/3}}{2\sqrt{12}\pi r_o^2};\ r_i = r_o \Big/ 2 \tag{6}$$

It should be noted that Eq. (5) and (6) are valid only for the condition $r_i = r_o/2$. However, in Eq. (5) and (6), it is seen that the coefficient of the material parameter does not change for $r_i = r_o/2$. By using this feature, ANN structures are developed independently of material properties. Thus, a model that can produce results with all kinds of materials has been put forward by training a network structure based on geometric parameters.

In this study, computer-aided design models of TLC diaphragms are designed with SOLIDWORKS software. Static Structural and Modal Analysis modules of ANSYS software are used for FEM analysis. Researchers and industry widely use ANSYS because the simulation results are very close to accurate results with mesh quality and computational ability. For this reason, it is frequently used in many diaphragm simulations [37-39].

To produce a model that satisfies all diaphragm geometries, the designed diaphragms must have different degrees of sensitivity. In the diaphragms, values of 5–20 μm with 5 μm steps are used for thickness (t) and 300–700 μm with 100 μm steps for outer radius (r_o). The inner radii (r_i) are approximated to the corresponding r_o value. Leaf angle (α) values are increased from 10° to 110° at intervals of 10°. The design parameters of the TLC diaphragm are tabulated in Table 1.

2.2. Constructing the ANN-based estimator

Although there are analytical solutions for basic geometries in diaphragm design, there are no analytical solutions for many designs. However, in many studies given in the literature, analytical expressions of diaphragms are clearly expressed depending on the material and geometric properties [16]. Both analytical equations and artificial intelligence-trained network structures are combined in a hybrid way for the first time in the literature. Thus, the parameters of TLC diaphragms are estimated with a material-independent ANN structure. The general working principle of the developed ANN-based estimator is given in Fig. 4.

As given in Fig. 4, different TLC structures are simulated for four geometric, three material parameters, and then the d and f obtained as a result of the simulation are determined as the output of the ANN. Then, to obtain material-independent geometric networks (gn_d, gn_f), the estimated networks (en_d, en_f) are multiplied by the coefficient depending on the material property given in Eq. (7).

$$gn_d = \frac{1}{dm_{sio2}} \times en_d,\quad gn_f = \frac{1}{fm_{sio2}} \times en_f \tag{7}$$

In this study, since the en_d and en_f networks are obtained for silica material, silica parameters are used in Eq. (2) and Eq. (4) to get dm_{SiO2} and fm_{SiO2} coefficients. Thus, material-independent geometric-network structures are obtained by using Eq. (8). Then the final TLC parameters are estimated by the following equation.

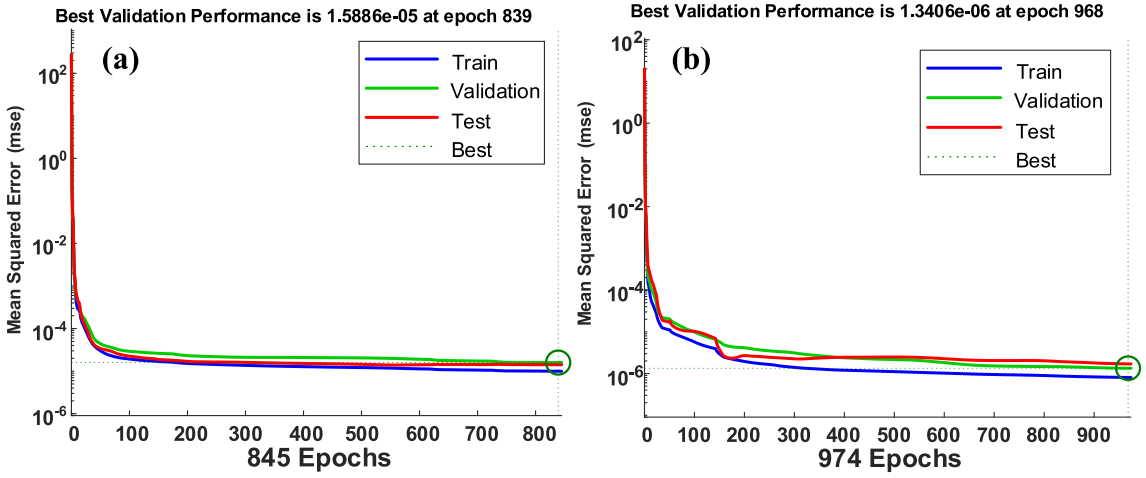

Fig. 6. Validation performances; **(a)** deflection "en_d", **(b)** frequency "en_f".

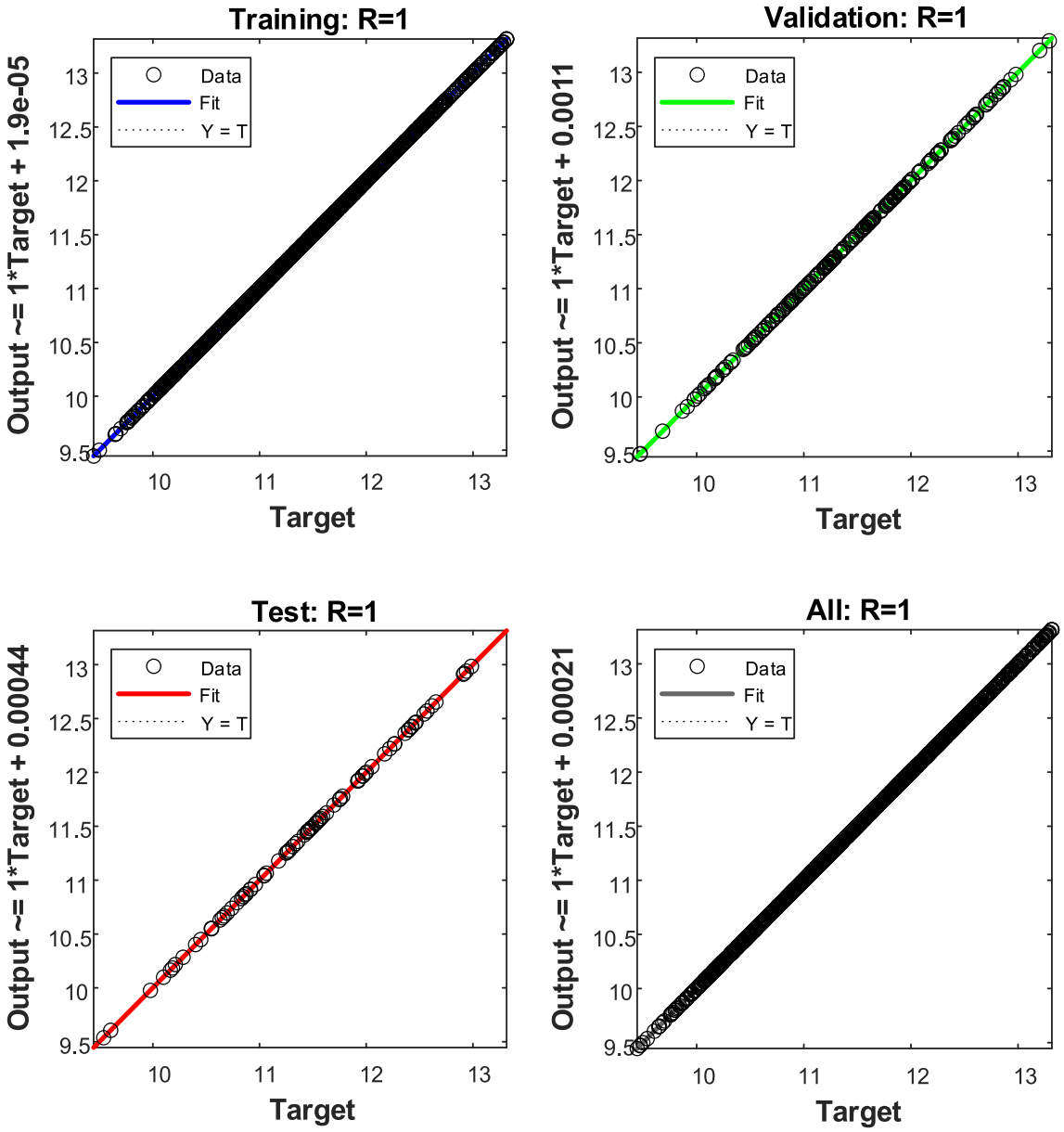

Fig. 7. Regression results for training, validation, and test processes.

Table 3
The training, validation, and test performances for ANN.

Metric	Train (1344 data)	Validation (252 data)	Test (84 data)
RMS (*d*)	6.707	8.680	4.970
MAPE (*d*)	0.238	0.400	0.149
RMS (*f*)	132.936	146.512	173.116
MAPE (*f*)	0.058	0.069	0.089

$$par_{est}: \begin{matrix} d_{est} = d_m \times gn_d \\ f_{est} = f_m \times gn_f \end{matrix} \quad (8)$$

The network's performance is given by mean absolute error (MAE).

2.2.1. Data matrix generation

SiO_2, one of the most popular diaphragm materials, is used to estimate TLC's d and f parameters. Since a material-independent network structure has been revealed thanks to the new method introduced in this study, there is no requirement for material selection. Using SiO_2 material parameters in Ansys software ($E = 73$ GPa, $\nu = 0.17$, $\rho = 2200$ kg/m^3), 1680 different TLCs are designed, and d and f parameters of each design are obtained. To create a uniformly spread data pool, t, r_o, r_i, and α are changed at different intervals, and the design parameters are also given in Table 1. Randomly selected 80% of the data is used for training, 15% for verification, and 5% for testing.

2.2.2. The ANN model

The ANN model consists of three layers, the input layer, the hidden layer, and the output layer [30,40]. There are four neurons in the input layer and one in the output layer. Since the number of neurons in the hidden layer affects the mean squared error (MSE) performance, the number of hidden layers is changed from 1 to 80 in the developed model, and the number of neurons with the best performance is found to be 52 as shown in Fig. 5. Although there are two output parameters in TLC parameter estimation, the ANN network is trained separately for each parameter, thus increasing the network's performance. The ANN model is trained with the Levenberg-Marquard learning algorithm. Epoc number and momentum parameter are determined as 1000 and 0.001,

Table 4
Comparison of the proposed model with the literature for designs providing $r_o/r_i = 2$ ratio.

Material	Material Parameters			Geometric Parameters				ANSYS results		ref [8] results		% error of ref [8]		Proposed method results		% error of proposed method	
	E (Pa)	ν	ρ (kg/m^3)	t (m)	r_o (m)	r_i (m)	α (°)	f (Hz)	d (m)	f (Hz)	d (m)	f (Hz)	d (m)	f (Hz)	d (m) @ 1 kPa	f (Hz)	d (m)
SiO_2	7.3E + 10	0.17	2200	0.00001	0.0003	0.00015	20	1.6735E + 05	4.8913E-08	1.6767E + 05	4.9488E-08	0.19	1.16	167320.568	4.88E-08	0.02	0.31
SiO_2	7.3E + 10	0.17	2200	0.00001	0.0003	0.00015	50	2.2600E + 05	3.0402E-08	2.2756E + 05	3.1299E-08	0.69	2.87	225912.055	3.05E-08	0.04	0.18
SiO_2	7.3E + 10	0.17	2200	0.00001	0.0003	0.00015	100	2.8801E + 05	2.1674E-08	2.8671E + 05	2.2132E-08	0.45	2.07	288036.257	2.16E-08	0.01	0.25
Si	1.63E + 11	0.27	2330	0.000005	0.0005	0.00025	20	4.4895E + 04	1.2750E-06	4.4849E + 04	1.3061E-06	0.10	2.38	45152.1799	1.27E-06	0.57	0.72
Si	1.63E + 11	0.27	2330	0.00002	0.0003	0.00015	50	6.6407E + 05	1.6422E-09	6.7633E + 05	1.6728E-09	1.81	1.83	664609.14	1.65E-09	0.08	0.64
Si	1.63E + 11	0.27	2330	0.000005	0.0007	0.00035	100	3.9947E + 04	2.1282E-06	3.9128E + 04	2.2439E-06	2.09	5.16	39619.0085	2.16E-06	0.82	1.58
Ag	7.60E + 10	0.39	10,490	0.000005	0.0007	0.00035	20	7.6619E + 03	9.6156E-06	7.7000E + 03	9.8422E-06	0.50	2.30	7777.90024	9.51E-06	1.51	1.09
Ag	7.60E + 10	0.39	10,490	0.00002	0.0003	0.00015	50	2.2375E + 05	3.1758E-09	2.2759E + 05	3.2812E-09	1.69	3.21	223645.669	3.24E-09	0.05	2.08
Ag	7.60E + 10	0.39	10,490	0.000005	0.0005	0.00025	100	2.6840E + 04	1.0856E-06	2.5807E + 04	1.1458E-06	4.00	5.25	26072.0086	1.11E-06	2.86	2.45
In_2Se_3	6.96E + 10	0.22	5800	0.00002	0.0005	0.00025	20	7.2711E + 04	4.8861E-08	7.3337E + 04	4.9058E-08	0.85	0.40	72923.6307	4.87E-08	0.29	0.38
In_2Se_3	6.96E + 10	0.22	5800	0.000015	0.0007	0.00035	50	3.7972E + 04	2.7164E-07	3.8087E + 04	2.8253E-07	0.30	3.86	37941.798	2.72E-07	0.08	0.17
In_2Se_3	6.96E + 10	0.22	5800	0.000005	0.0007	0.00035	100	1.6252E + 04	5.1683E-06	1.5996E + 04	5.3941E-06	1.60	4.19	16196.2495	5.20E-06	0.34	0.55
EPDM	4.47E + 10	0.38	860	0.000005	0.0007	0.00035	20	2.0439E + 04	1.6499E-05	2.0531E + 04	1.6886E-05	0.45	2.29	20738.8553	1.63E-05	1.47	1.10
EPDM	4.47E + 10	0.38	860	0.00002	0.0003	0.00015	50	5.9636E + 05	5.4589E-09	6.0684E + 05	5.6294E-09	1.73	3.03	596324.849	5.56E-09	0.01	1.88
EPDM	4.47E + 10	0.38	860	0.000005	0.0003	0.00015	100	1.9349E + 05	2.4429E-07	1.9114E + 05	2.5476E-07	1.23	4.11	192658.452	2.48E-07	0.43	1.55
Graphene	1.00E + 12	0.165	2200	0.00002	0.0005	0.00025	20	4.4461E + 05	3.4632E-09	4.4642E + 05	3.4904E-09	0.41	0.78	443902.239	3.46E-09	0.16	0.00
Graphene	1.00E + 12	0.165	2200	0.000015	0.0003	0.00015	50	1.2475E + 06	6.6418E-10	1.2623E + 06	6.7816E-10	1.17	2.06	1247266.57	6.65E-10	0.02	0.07
Graphene	1.00E + 12	0.165	2200	0.00002	0.0005	0.00025	100	7.6564E + 05	1.5328E-09	7.6337E + 05	1.5610E-09	0.30	1.80	766464.218	1.53E-09	0.11	0.02
											MAPE	**1.09**	**2.71**		**MAPE**	**0.49**	**0.83**

Table 5
Comparison of the proposed model with the literature for designs without radius constraints.

Material	Material Parameters			Geometric Parameters				ANSYS results		ref [8] results		% error for ref [8]		Proposed method results		% error of proposed method	
	E (Pa)	*ν*	*ρ* (kg/m^3)	*t* (m)	r_o (m)	r_i (m)	*α*(°)	*f* (Hz)	*d* (m)	*f* (Hz)	*d* (m)	*f* (Hz)	*d* (m)	*f* (Hz)	*d* (m)	*f* error	*d* error
SiO_2	7.3E + 10	0.17	2200	0.000005	0.0003	0.0001	40	110,130	2.5117E-07	105623.4722	2.7995E-07	4.09	11.46	110250.025	2.51E-07	0.11	0.00
SiO_2	7.3E + 10	0.17	2200	0.000005	0.0003	0.0002	20	83,696	4.1435E-07	83833.40541	3.9591E-07	0.16	4.45	83734.2619	4.15E-07	0.05	0.09
SiO_2	7.3E + 10	0.17	2200	0.000005	0.0004	0.00005	80	75,338	6.6914E-07	74855.94522	6.2563E-07	0.64	6.50	75235.1859	6.70E-07	0.14	0.06
SiO_2	7.3E + 10	0.17	2200	0.000005	0.0006	0.00025	100	36,161	2.7557E-06	35838.27669	2.8329E-06	0.89	2.80	36134.0634	2.76E-06	0.07	0.01
SiO_2	7.3E + 10	0.17	2200	0.000005	0.0007	0.00005	10	20,005	8.7997E-06	12221.37881	1.6596E-05	38.91	88.60	19984.2767	8.84E-06	0.10	0.43
SiO_2	7.3E + 10	0.17	2200	0.00001	0.0004	0.00005	10	107,240	1.3335E-07	74855.94522	2.2119E-07	30.20	65.87	107258.052	1.33E-07	0.02	0.30
Si	1.63E + 11	0.27	2330	0.000015	0.0007	0.0003	60	100,000	1.0056E-07	99005.57468	1.0729E-07	0.99	6.70	99978.0077	1.01E-07	0.02	0.64
Si	1.63E + 11	0.27	2330	0.000015	0.0007	0.0005	120	125,220	7.5249E-08	124739.2076	7.5868E-08	0.38	0.82	125017.18	7.60E-08	0.16	0.95
Si	1.63E + 11	0.27	2330	0.000015	0.0007	0.00055	10	58,669	2.6405E-07	54484.86747	2.6281E-07	7.13	0.47	59067.271	2.66E-07	0.68	0.77
Ag	7.60E + 10	0.39	10,490	0.000005	0.0003	0.0001	20	4.3796E + 04	2.9679E-07	41922.36066	3.3203E-07	4.28	11.88	44786.0964	2.88E-07	2.26	2.96
Ag	7.60E + 10	0.39	10,490	0.000005	0.0005	0.00015	20	1.6169E + 04	2.2073E-06	15092.04984	2.5620E-06	6.66	16.07	16529.0489	2.13E-06	2.23	3.32
Ag	7.60E + 10	0.39	10,490	0.00001	0.0003	0.0001	20	8.6703E + 04	3.7829E-08	83844.72132	4.1504E-08	3.30	9.72	88958.5076	3.63E-08	2.60	3.96
In_2Se_3	6.96E + 10	0.22	5800	0.000005	0.0003	0.0001	20	5.4171E + 04	3.5418E-07	50928.67787	4.0691E-07	5.99	14.89	54407.6392	3.53E-07	0.44	0.34
In_2Se_3	6.96E + 10	0.22	5800	0.00001	0.0005	0.00045	100	6.4191E + 04	1.7134E-07	62702.50619	1.7552E-07	2.32	2.44	64003.7259	1.72E-07	0.29	0.30
In_2Se_3	6.96E + 10	0.22	5800	0.00002	0.0005	0.00045	100	1.2789E + 05	2.1564E-08	125405.0124	2.1940E-08	1.94	1.74	127466.088	2.17E-08	0.33	0.52
EPDM	4.47E + 10	0.38	860	0.000005	0.0003	0.0001	20	1.1689E + 05	5.0850E-07	111781.0394	5.6966E-07	4.37	12.03	119416.853	4.94E-07	2.16	2.83
EPDM	4.47E + 10	0.38	860	0.000005	0.0005	0.00015	20	4.3148E + 04	3.7829E-06	40241.17417	4.3955E-06	6.74	16.19	44072.763	3.66E-06	2.14	3.22
EPDM	4.47E + 10	0.38	860	0.00002	0.0003	0.0002	50	5.9738E + 05	5.6450E-09	606840.8449	5.6294E-09	1.58	0.28	592938.008	5.86E-09	0.74	3.88
Graphene	1.00E + 12	0.165	2200	0.00001	0.0003	0.0001	20	6.5811E + 05	3.1686E-09	620028.2112	3.6189E-09	5.79	14.21	657844.447	3.17E-09	0.04	0.03
Graphene	1.00E + 12	0.165	2200	0.00002	0.0003	0.0002	50	1.6435E + 06	2.9786E-10	1683015.499	2.8610E-10	2.40	3.95	1644457.3	2.98E-10	0.06	0.05
Graphene	1.00E + 12	0.165	2200	0.00002	0.0003	0.00025	100	2.1306E + 06	2.0358E-10	2120466.655	2.0230E-10	0.48	0.63	2130245.57	2.04E-10	0.02	0.09
											MAPE	**6.15**	**13.89**		**MAPE**	**0.70**	**1.18**

respectively. All parameters are given in Table 2.

3. Results and discussions

80% of the 1680 designs are used as training, 15% as validation and the remaining 5% as testing to estimate the en_d and en_f values of the TLC diaphragms. Since the maximum validation error (max_fail) is defined as 6 in the developed network, the training stops if the network performance in the validation vectors does not increase or remains the same in successive max_fail periods. Therefore, the maximum number of epochs may not always be reached in the verification process. Validation performance graphs for both en_d and en_f are given in Fig. 6. As seen in Fig. 6a, the en_d value reached the best validation value after 839 iterations, while the en_f value reached the best validation value after 968 iterations, as seen in Fig. 6b. Training, validation, and test regression results for both parameters are found to be 1, and the results are given in Fig. 7. RMS and MAPE values for training, validation, and testing processes are given in Table 3.

When the results in Table 3 are evaluated, it is seen that both *d* and *f* values are estimated with very high performance. The trained network data is shared in supplementary files for the developed network structure to be used in further studies by other researchers. Thus, if any material's properties and geometry parameters are defined in the attached Matlab file, the *d* and *f* values of the desired diaphragm can be easily estimated.

Although there is no network model or analytical solution developed for a general TLC structure in the literature, an empirical formula is developed for the ratio $r_o/r_i = 2$ [16]. The performance of the network structure developed is compared with the literature. The performance of the developed network is compared with some test data that are not used in training and validation processes and provided the ratio $r_o/r_i = 2$. The performance of the developed network is given in Table 4.

When Table 4 is examined, it is seen that the proposed method estimates the *d* and *f* parameters with much higher precision than the result obtained in [16]. Also, it should be noted that the equation given in [16] is valid only for the ratio $r_o/r_i = 2$, and for other cases, the error rate is too high. The method proposed in this study can produce results in all geometries without any geometric restrictions, and Table 5 presents the results for different materials.

Table V shows that the network trained only for SiO_2 produces very close results to the actual value for all kinds of materials with the suggested coefficient multiplier. These results have brought a new approach to diaphragm design, and it has been demonstrated that different material responses can be obtained with diaphragms designed for a certain number of a single material. Two FEM results are depicted in Fig. 8 compared to ANN results given in Table V.

4. Conclusion

In this study, the *d* and *f* parameters of TLC type DDs are estimated by ANN for diaphragm-based fiber-optic Fabry-Perot sensors. Firstly, FEM analysis data of 1680 different TLC diaphragms designed for SiO_2 material are obtained. Randomly selected 1344 data are used for training, 252 for verification, and 84 for testing.

Two different networks are trained to estimate *d* and *f* parameters of the TLC diaphragms. In the training of the networks, four different geometric parameters such as radius, diameter, thickness, and angle are used as inputs. The effect of the material parameters of the diaphragm is added to the model with a multiplier coefficient. Thus, the *d* and *f* values of TLC diagrams produced with all kinds of materials are estimated to be very accurate.

The performance of the proposed model is compared with an empirical equation given in the literature, which is valid only for the $r_o/r_i = 2$ condition. For 18 TLC diaphragms designed with six different materials, with the equation given in [16], the MAPE values of *d* and *f* are 2.71 and 1.09, respectively. In contrast, the MAPE values of the

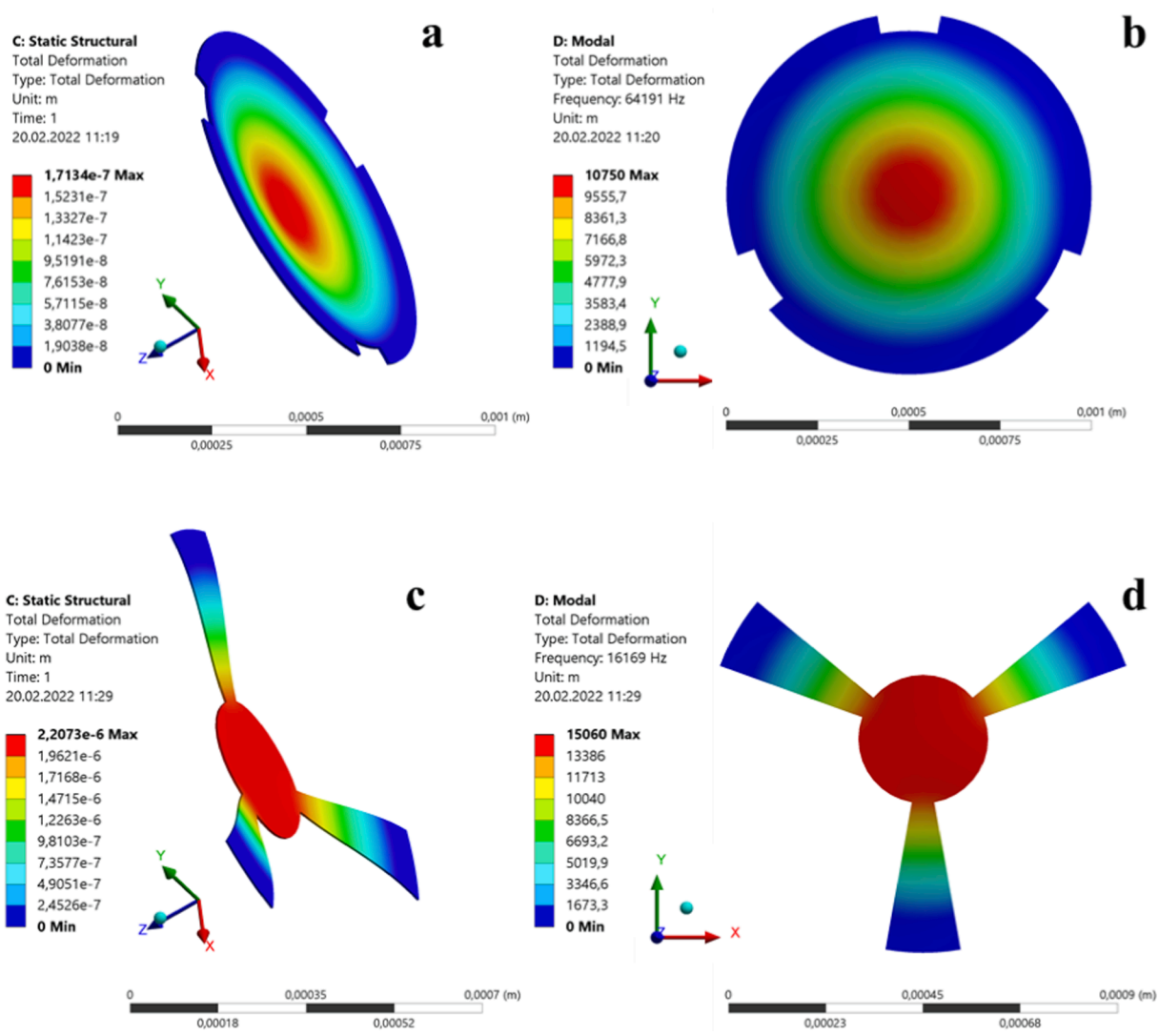

Fig. 8. ANSYS results of TLC diapragm: **(a)** static structural and **(b)** modal analysis for In_2Se_3 ($t = 10$ μm, $r_o = 500$ μm, $r_i = 450$ μm, $\alpha = 100$) and **(c)** static structural and **(d)** modal analysis for Ag ($t = 5$ μm, $r_o = 500$ μm, $r_i = 150$ μm, $\alpha = 20$).

model proposed in this study are obtained as 0.83 and 0.49, respectively. These results clearly show that the d and f parameters of the TLC diaphragms can be estimated quickly, with very close to actual values, without long design and simulation processes.

It is obvious that not every nonlinear problem can be solved by every ML method. In this study, the feasibility of parameter estimation of design diaphragms with ANN has been demonstrated for the first time in the literature. The ANN model presented in this study can be easily used in Fabry-Perot interferometers and other structures such as membranes, resonators, microphones, piezoelectrics, and transducers. For this reason, the proposed ANN model is promising, and it can be applied to different DDs for other purposes by designers.

CRediT authorship contribution statement

Enes Yigit: Methodology, Software, Validation, Writing – original draft. **Şekip Esat Hayber:** Data curation, Formal analysis, Visualization, Writing – original draft. **Umut Aydemir:** Conceptualization, Writing – review & editing.

Declaration of Competing Interest

The authors declare that they have no known competing financial interests or personal relationships that could have appeared to influence the work reported in this paper.

Acknowledgment

This study is supported by the Scientific Research Projects Units of Bursa Uludağ University, with grant number of FOA-2021-630.

Appendix A. Supplementary material

Supplementary data to this article can be found online at https://doi.org/10.1016/j.measurement.2022.111534.

References

[1] B.H. Lee, Y.H. Kim, K.S. Park, J.B. Eom, M.J. Kim, B.S. Rho, H.Y. Choi, Interferometric Fiber Optic sensors, Interferometric fiber optic sensors. sensors 12 (3) (2012) 2467–2486.
[2] Udd, E., & Spillman Jr, W. B. (Eds.). (2011). Fiber optic sensors: an introduction for engineers and scientists. John Wiley & Sons.
[3] H.F. Taylor, Fiber optic sensors based upon the Fabry-Perot interferometer, Vol. 41, Marcel Dekker, New York, 2002.
[4] J. Ma, H. Xuan, H.L. Ho, W. Jin, Y. Yang, S. Fan, Fiber-optic Fabry-Pérot acoustic sensor with multilayer graphene diaphragm, IEEE Photonics Technol. Lett. 25 (10) (2013) 932–935.

[5] J. Eom, C.J. Park, B.H. Lee, J.H. Lee, I.B. Kwon, E. Chung, Fiber optic Fabry-Perot pressure sensor based on lensed fiber and polymeric diaphragm, Sens. Actuators, A 225 (2015) 25–32.

[6] H. Moradi, P. Parvin, A. Ojaghloo, F. Shahi, Ultrasensitive fiber optic Fabry Pérot acoustic sensor using phase detection, Measurement 172 (2021) 108953.

[7] C. Li, S. Lu, C. Zhong, X. Song, High-sensitivity low-frequency Fabry-Perot ultrasonic hydrophone with chitosan diaphragm, IEEE Sens. J. 22 (7) (2022) 6669–6676.

[8] H. Zhang, Q. Jiang, Highly sensitive air pressure sensor based on Fabry-Perot interference (January 2022), IEEE Sens. J. (2022).

[9] Y. Qi, M. Zhao, B. Li, Z. Ren, B. Li, X. Wei, A Compact Optical MEMS Pressure Sensor Based on Fabry-Pérot Interference, Sensors 22 (5) (2022) 1973.

[10] Ş.E. Hayber, U. Aydemir, T.E. Tabaru, Ö.G. Saraçoğlu, The experimental validation of designed fiber optic pressure sensors with EPDM diaphragm, IEEE Sens. J. 19 (14) (2019) 5680–5685.

[11] L. Liu, P. Lu, S. Wang, X. Fu, Y. Sun, D. Liu, Q. Yao, UV adhesive diaphragm-based FPI sensor for very-low-frequency acoustic sensing, IEEE Photonics J. 8 (1) (2015) 1–9.

[12] Z. Gong, K. Chen, Y. Yang, X. Zhou, Q. Yu, Photoacoustic spectroscopy based multi-gas detection using high-sensitivity fiber-optic low-frequency acoustic sensor, Sens. Actuators, B 260 (2018) 357–363.

[13] Z. Gong, K. Chen, Y. Yang, X. Zhou, W. Peng, Q. Yu, High-sensitivity fiber-optic acoustic sensor for photoacoustic spectroscopy based traces gas detection, Sens. Actuators, B 247 (2017) 290–295.

[14] Wang, W., Yu, Q., & Jiang, X. (2012). High sensitivity diaphragm based extrinsic Fabry-Pérot interferometric optical fiber underwater ultrasonic sensor. Optoelectronics and Advanced Materials-Rapid Communications, 6(July-August 2012), 697-702.

[15] D. Duraibabu, S. Poeggel, E. Omerdic, R. Capocci, E. Lewis, T. Newe, G. Leen, D. Toal, G. Dooly, An optical fibre depth (pressure) sensor for remote operated vehicles in underwater applications, Sensors 17 (2) (2017) 406.

[16] S.E. Hayber, T.E. Tabaru, O.G. Saracoglu, A novel approach based on simulation of tunable MEMS diaphragm for extrinsic Fabry-Perot sensors, Opt. Commun. 430 (2019) 14–23.

[17] C. Fu, W. Si, H. Li, D. Li, P. Yuan, Y. Yu, A novel high-performance beam-supported membrane structure with enhanced design flexibility for partial discharge detection, Sensors 17 (3) (2017) 593.

[18] H. Li, H. Deng, G. Zheng, M. Shan, Z. Zhong, B. Liu, Reviews on corrugated diaphragms in miniature fiber-optic pressure sensors, Appl. Sci. 9 (11) (2019) 2241.

[19] Y. Sun, G. Feng, G. Georgiou, E. Niver, K. Noe, K. Chin, Center embossed diaphragm design guidelines and Fabry-Perot diaphragm fiber optic sensor, Microelectron. J. 39 (5) (2008) 711–716.

[20] Ş.E. Hayber, U. Aydemir, Design and simulation of a novel fungus-shaped center embossed diaphragm for fiber optic pressure sensors, Optical Fiber Technol. 61 (2021) 102429.

[21] J. Liu, L. Yuan, J. Lei, W. Zhu, B. Cheng, Q.i. Zhang, Y. Song, C. Chen, H. Xiao, Micro-cantilever-based fiber optic hydrophone fabricated by a femtosecond laser, Opt. Lett. 42 (13) (2017) 2459.

[22] H. Li, J. Bu, W. Li, J. Lv, X. Wang, K. Hu, Y. Yu, Fiber optic Fabry-Perot sensor that can amplify ultrasonic wave for an enhanced partial discharge detection, Sci. Rep. 11 (1) (2021) 1–6.

[23] H. Li, X. Wang, D. Li, J. Lv, Y. Yu, MEMS-on-fiber sensor combining silicon diaphragm and supporting beams for on-line partial discharges monitoring, Opt. Express 28 (20) (2020) 29368–29376.

[24] H. Li, J. Lv, D. Li, C. Xiong, Y. Zhang, Y. Yu, MEMS-on-fiber ultrasonic sensor with two resonant frequencies for partial discharges detection, Opt. Express 28 (12) (2020) 18431–18439.

[25] X. Qi, S. Wang, J. Jiang, K. Liu, P. Zhang, R. Li, T. Liu, Flywheel-like diaphragm-based fiber-optic Fabry-Perot frequency tailored acoustic sensor, J. Phys. D Appl. Phys. 53 (41) (2020) 415102.

[26] X. Qi, S. Wang, J. Jiang, K. Liu, P. Zhang, Z. Li, T. Liu, Study on the sensitization effect of Flywheel-Like diaphragm on fiber-optic Fabry-Perot acoustic sensor, IEEE Access 8 (2020) 99286–99293.

[27] W. Fan, J. Wen, H. Gao, X. Qiao, Low-frequency fiber bragg grating accelerometer based on diaphragm-type cantilever, Optical Fiber Technol. 70 (2022) 102888.

[28] M. Farajollahi, M. Goharzay, D. Borzuei, S.F. Moosavian, Stress, sensitivity and frequency analysis of the corrugated diaphragm for different corrugation structures, Smart Struct. Systems, An Int. J. 27 (5) (2021) 837–846.

[29] E. Yigit, Operating frequency estimation of slot antenna by using adapted kNN algorithm, Int. J. Intelligent Systems and Appl. Eng. 6 (1) (2018) 29–32.

[30] E. Yigit, A. Kayabasi, A. Toktas, K. Sabanci, A neurocomputational model for estimating the triple-frequency of T-shaped patch antennas, Microwave Opt. Technol. Lett. 61 (6) (2019) 1590–1597.

[31] S. Keser, Ş.E. Hayber, Fiber optic tactile sensor for surface roughness recognition by machine learning algorithms, Sens. Actuators, A 332 (2021), 113071.

[32] Y. Yang, O.A. Jiménez-Negrón, J.R. Kitchin, Machine-learning accelerated geometry optimization in molecular simulation, J. Chem. Phys. 154 (23) (2021) 234704.

[33] R. Phellan, B. Hachem, J. Clin, J.M. Mac-Thiong, L. Duong, Real-time biomechanics using the finite element method and machine learning: review and perspective, Med. Phys. 48 (1) (2021) 7–18.

[34] F. Xu, D. Ren, X. Shi, C. Li, W. Lu, L.u. Lu, L. Lu, B. Yu, High-sensitivity Fabry-Perot interferometric pressure sensor based on a nanothick silver diaphragm, Opt. Lett. 37 (2) (2012) 133.

[35] Cheng, L., Qianwen, L., Tingting, G., Jun, X., Shangchun, F., & Wei, J. (2015, November). An ultra-high sensitivity Fabry-Perot acoustic pressure sensor using a multilayer suspended graphene diaphragm. In 2015 IEEE SENSORS (pp. 1-4). IEEE.

[36] J. Deng, H. Xiao, W. Huo, M. Luo, R. May, A. Wang, Y. Liu, Optical fiber sensor-based detection of partial discharges in power transformers, Opt. Laser Technol. 33 (5) (2001) 305–311.

[37] W.J. Wang, R.M. Lin, D.G. Guo, T.T. Sun, Development of a novel Fabry-Perot pressure microsensor, Sens. Actuators, A 116 (1) (2004) 59–65.

[38] M. Gutierrez-Rivera, D. Jauregui-Vazquez, D.F. Garcia-Mina, J.M. Sierra-Hernandez, J.M. Estudillo-Ayala, M. Almanee, R. Rojas-Laguna, Fiber Optic Fabry-Perot micro-displacement sensor based on low-cost polymer film, IEEE Sens. J. 20 (9) (2019) 4719–4725.

[39] J. Liu, P. Jia, H. Zhang, X. Tian, H. Liang, Y. Hong, T. Liang, W. Liu, J. Xiong, Fiber-optic Fabry-Perot pressure sensor based on low-temperature co-fired ceramic technology for high-temperature applications, Appl. Opt. 57 (15) (2018) 4211.

[40] S. Haykin, Neural networks: a comprehensive foundation, Macmillan College Publishing Company, New York, A.B.D., 1994.